An investigation of infrasound propagation over mountain ranges

Florentin Damiens, Christophe Millet, François Lott

An investigation of infrasound propagation over mountain ranges

Florentin Damiens,[1] Christophe Millet,[1,a] François Lott[2]

[1] Commissariat à l'Énergie Atomique et aux Énergies Alternatives, 91297 Arpajon, France

[2] Laboratoire de Météorologie Dynamique, École Normale Supérieure, 75231 Paris, France

[a] Also at: Centre de Mathématiques et Leurs Applications, École Normale Supérieure Paris-Saclay, 94235 Cachan, France. Electronic mail: christophe.millet@cea.fr.

Abstract

Linear theory is used to analyze trapping of infrasound within the lower tropospheric waveguide during propagation above a mountain range. Atmospheric flow produced by the mountains is predicted by a nonlinear mountain gravity wave model. For the infrasound component, we solve the wave equation under the effective sound speed approximation using both a finite difference method and a WKB approach. It is shown that in realistic configurations, the mountain waves can deeply perturb the low level waveguide, which leads to significant acoustic dispersion. To interpret these results each acoustic mode is tracked separately as the horizontal distance increases. It is shown that during statically stable situations, situations that are common during night over land in winter, the mountain waves induce a strong Foehn effect downstream, which shrinks the waveguide significantly. This yields a new form of infrasound absorption, that can largely outweigh the direct effect the mountain induces on the low level waveguide. For the opposite case, when the low level flow is less statically stable (situations that are more common during day in summer), mountain wave dynamics do not produce dramatic responses downstream. It may even favor the passage of infrasound and mitigate the direct effect of the obstacle.

I. Introduction

Infrasound, which is defined as sound waves that are lower in frequency than 20 Hz, is characterized by an ability to travel over long horizontal distances in the atmosphere. This is related to the fact that the wind and temperature strongly vary with altitude, providing multiple ducts in which infrasound can propagate efficiently[20]. Although an important duct is potentially in the lower thermosphere, as a result of the steep increase in temperature (e.g. above 90 km), the decrease in mean density produces substantial absorption coefficients there[42]. For this reason, the most efficient ducts are often within the middle atmosphere, e.g. above the tropopause at around 20 km and below the mesopause at 90 km. At lower altitudes, infrasound can also be trapped within tropospheric waveguides over distances that may reach several hundred of kilometers, at least when the weather conditions permit[43;31]. However in this case, the wave interacts with the ground surface much more than wave refracting higher in the atmosphere and topographic features produce quantifiable effects on the recorded data[30]. Furthermore, at these altitudes the absorption coefficient is small and thus, it is neglected in most practical applications.

Although much less studied, the propagation of infrasound over distances of a few tens of kilometers can be controlled by a planetary boundary layer duct[11;45], which is a region of approximately 1 km depth in which the boundary effects are reflected in the flow[16]. For these relatively short propagation ranges, the upward refraction at higher altitudes (around

and above the tropopause) can be ignored[45] and the acoustic field can be described by a modal expansion involving a few modes. For completeness, it is important to note that the absorption properties of ground play a significant role[4], in the sense that vegetation-covered land absorbs more energy than bare-ground for instance. We know that some modes are sensitive to such absorptions[44;47] but we will not include these effects here, essentially because a comprehensive theory of acoustic propagation which accounts for both absorption by vegetation and turbulence is lacking.

The common approach to calculate infrasound propagation in the atmosphere consists in solving the acoustic equation in a given background atmospheric state that varies with altitude and horizontal distance. This approach captures the most significant ducts, but sometimes it fails in predicting important arrivals[17;3;34]. The reason is that the atmospheric specifications, that are issued from operational numerical weather forecasts (e.g., provided by the ECMWF Integrated Forecast System or the NOAA Global Forecast System) or atmospheric climate reanalysis (e.g., ERA-Interim or NASA Modern Era Retrospective Reanalysis for Research and Applications), are associated with spatial resolutions that are much larger than the typical infrasound wavelength. These products therefore fail in representing important small-scale atmospheric fluctuations that can substantially modify the larger-scale ducts[6], especially for borderline ducts that barely return sound to the ground. The statistics of these fluctuations, however, are poorly understood, whereas their knowledge is required

for infrasound propagation modeling. For instance, Chunchuzov *et al.*[12] have shown the need to introduce random atmospheric perturbations to adequately represent the acoustic properties of the boundary layer, but in their work the sources of perturbations are not specified. As in the troposphere the (unresolved) fluctuations are mainly produced by mountains[18], the contribution of these mountains to infrasound propagation remains an important open question.

In a first attempt to incorporate topography effects in acoustic propagation, high-resolution terrain models have been used to represent the lower boundary by a sequence of up and down stair steps[2;30]. In this approach, mountains directly modify the altitude of the lower boundary of the troposphere, which affects the acoustic cut-off frequencies of the corresponding ducts. This can be viewed as applying a "mask" onto the atmospheric specifications, and ignoring the direct influence of the mountain ridges on the local wind and temperature fields. This is an extremely serious limitation, given that mountains can dynamically produce very intense phenomena, like downslope winds, Foehn, or trapped lee waves[40;15]. As an illustration, it is worth mentioning that even small "mountains", with elevations of a several hundred meters, can develop substantial winds and temperature disturbances, depending on the incoming flow structure[15].

There are two primary objectives in the present investigation. The first is to compare the results of the "mask" approximation to that obtained with a wind model that captures

the interaction between the topography and the boundary layer. The second objective is to examine the physical mechanisms that cause a low-level acoustic duct to be affected and eventually destroyed by mountain-induced disturbances. Here we use the mountain flow model described by Lott[29]. With respect to our first objective, this model involves a nonlinear boundary condition, *i.e.* it includes an obstacle that penetrates inside the low level waveguide and reduces its depth, an effect that potentially recovers the classical "mask" technique. It is worth while to point out that the model also predicts a mountain wave field, which compares in amplitude to the background winds and temperature variations responsible for the waveguide. This inherently affects the trapped acoustic modes, yielding highly dispersed signals as well as irreversible absorption of the acoustic wave passing over the ridge.

The paper is organized as follows. In section II, the mountain wave model is described and the dominant features of the mountain wave field are discussed in terms of dimensionless Richardson and Froude numbers. The effect of mountain wave disturbances on the acoustic field $p(x, z)$ is then considered in section III, using a classical range-dependent normal mode approach[24] to account for flow changes along the source-receiver distance x. To make the absorptive properties more transparent, the acoustic modes are also obtained using a WKB approximation. In section IV, it is found that the interaction between the mountain flow and the acoustic field gives rise to attenuation or amplification of ground-based signals,

depending on the statical stability of the boundary layer flow. The characteristics of the perturbed acoustic modes such as phase velocities, attenuations, and wave structures in the (x, z)-plane are provided and discussed. In section V, the downstream attenuation is systematically evaluated in terms of dimensionless numbers that control the mountain flow dynamics. Importantly, it is found that in near-neutral conditions, the mountain wave dynamics can favor infrasound propagation above the mountain, mitigating the direct effect of the obstacle.

II. Atmospheric mountain flow model

A. Formalism

Mountain waves, that occur when a stably stratified flow is forced by an obstacle, are often standing or nearly so, at least to the extent that the upstream environmental conditions are stationary. They can accompany Foehn wind conditions that are characterized by warm and dry downslope winds on the lee side of mountains[37]. In the present study, we use the mountain wave model developed by Lott[29], which is adapted from Long[27]'s model to incoming shear flows that varies with altitude. Comparisons with nonlinear simulations[13] demonstrated that this model is well-suited for capturing realistic features of mountain flow dynamics.

In the present study, the mean state consists of an isothermal atmosphere, at temper-

ature T_0, in the presence of a background wind $U(z)$ which is assumed to be in the shape of an hyperbolic tangent function. This representation is appropriate to describe the planetary boundary layers[8;10] and can even be used to initialize mesoscale models[35]. Although such a profile can occur during strong stratification or above the lowest maximum of the wind speed[32], there are many other semi-empirical models that adequately describe the wind shear. Here, the profile is used to mimic the incoming boundary layer, so that stationary gravity waves can be generated through interaction with the mountain, as observational evidence[9;41] suggest. Specifically, the mean flow is given by

$$T(z) = T_0, \quad U(z) = U_0 \tanh(z/\delta), \tag{1}$$

where δ is the boundary layer thickness, U_0 denotes the maximum wind speed over the mountain, and z is the height, which is here typically smaller than 5 km. The thermodynamic sound speed c_0 is given by $c_0^2 = \gamma R T_0$, where γ is the ratio of specific heats and R is the specific gas constant for dry air. Hence, in an isothermal atmospheric boundary layer, the sound speed is constant. Using the ideal gas law and hydrostatic balance we know that in an isothermal atmosphere the background pressure and density vary as $\exp(-gz/RT_0)$, and the background potential temperature θ is related to the Brunt-Väisälä frequency[20] N through

$$N^2 = \frac{g}{\theta}\frac{d\theta}{dz} = \frac{\gamma - 1}{\gamma}\frac{g^2}{RT_0}, \tag{2}$$

where g is the gravitational constant. Solving (2), we observe that θ varies as $\exp(N^2 z/g)$,

which provides the stratification needed for internal gravity waves to develop.

Now, given this stratification (through N), it is conventional to neglect the vertical changes of background density for relatively small δ (typically less than 1 km). This is the classical Boussinesq approximation, that we can adopt here because our focus lies on the low level waveguide. Within the framework of the above hypothesis, and following previous works[29], the vertical perturbation in the velocity is given by the (inverse) Fourier transform

$$w'(x,z) = \int_{\mathbb{R}} f(k)\hat{w}_c(k,z)\mathrm{e}^{ikx}\,\mathrm{d}k, \tag{3}$$

where $f(k)$ is an amplitude function that depends on the wavenumber k, and $\hat{w}_c(k,z)$ is a canonical solution satisfying the Taylor-Goldstein equation

$$\frac{\mathrm{d}^2\hat{w}_c}{\mathrm{d}z^2} + \left[\frac{N^2}{U^2} - \frac{U_{zz}}{U} - k^2\right]\hat{w}_c = 0, \tag{4}$$

with the condition $\hat{w}_c(k,z) \sim \mathrm{e}^{-\lambda(k)z}$, as $z \to \infty$, and where the square-root function λ is defined by

$$\lambda(k) = \left[k^2 - \frac{N^2}{U_0^2}\right]^{\frac{1}{2}}. \tag{5}$$

In order that the boundedness or outgoing-wave condition be satisfied as $z \to \infty$, the branch cuts of λ are inserted such that we have $\hat{w}_c(k,z) \sim \mathrm{e}^{i\epsilon\lambda(k)z}$ where $\epsilon = \mathrm{sign}(k)$ is to ensure upward propagation for $|k| < N/U_0$.

The boundary condition at $z \to \infty$ and the choice of branch cuts allow the solution of (4) to be expressed in terms of hypergeometric functions. A dynamically consistent horizontal

velocity field u' can be obtained in spectral space using a polarization relation[18]. The amplitude $f(k)$ is then determined through inversion of the "free-slip" nonlinear boundary condition

$$w'(x, h(x)) = [U(h) + u'(x, h(x))] \frac{dh}{dx}, \tag{6}$$

with the witch of Agnesi profile

$$h(x) = \frac{H}{1 + \frac{x^2}{2L^2}}, \tag{7}$$

where H is the ridge top height and L is a characteristic length scale. Application of the Fourier transform to (7) leads to $\hat{h}(k) = HL\mathrm{e}^{-k\sqrt{2}L}/\sqrt{2}$, which implies that the dominant horizontal wavelength is given by $k = 1/\sqrt{2}L$. In the following, this profile will be centred at $x_0 = 25$ km and we will use $h(x)$ instead of $h(x - x_0)$ for notational conciseness.

To describe the flow response, it is also worthwhile to use the three dimensionless parameters

$$J = \frac{N^2\delta^2}{U_0^2}, \quad H_N = \frac{NH}{U_0}, \quad \text{and} \quad F = \frac{NL}{U_0}. \tag{8}$$

While the Richardson number J measures the background flow stability[33;23], the other parameters are related to the shape of the mountain. The parameter H_N is a dimensionless mountain height that measures the degree of nonlinearity in the flow response[39]. The classical Froude number F compares the advective time-scale to cross the ridge and the buoyancy oscillation time-scale. This last parameter measures the significance of non-hydrostatic effects[36]. In the following we will fix N, U_0 and L such that $F = 10 \gg 1$, a value that

guarantees that no substantial trapped lee waves are forced. We will vary the boundary layer depth δ and/or the mountain height H.

B. Effective sound speed disturbances

Following Waxler[44] we next use the effective sound speed approximation[19], in which the component of the horizontal wind speed in the direction of propagation is added to the thermodynamic sound speed. For an isothermal atmosphere, with a varying background wind U, this approximation yields $c(z) = c_0 + U(z)$ and thus, ducting is only due to the change in altitude of U. Hence, in presence of temperature and wind fluctuations, the perturbed effective sound speed is given by

$$c_0\sqrt{1+\frac{T'}{T_0}} + U + u'. \tag{9}$$

where the temperature and the horizontal wind perturbations, which are denoted by T' and u', respectively, are obtained from the vertical velocity w' using polarization relations[18].

In order to illustrate how mountain waves can perturb the background state, the mountain wave model described in section II.A is used with parameters that are representative of the lower troposphere. Here, and in the following, we consider a boundary layer flow at $U_0 = 10$ m.s^{-1} in a stratified medium characterized by $N = \sqrt{2}.10^{-2}$ s^{-1}, and take $L = 10$ km to enforce $F = 10$. For illustrative purposes, the height of the mountain and the boundary layer thickness are fixed to $H = 350$ m and $\delta = 860$ m, respectively. For these parameters,

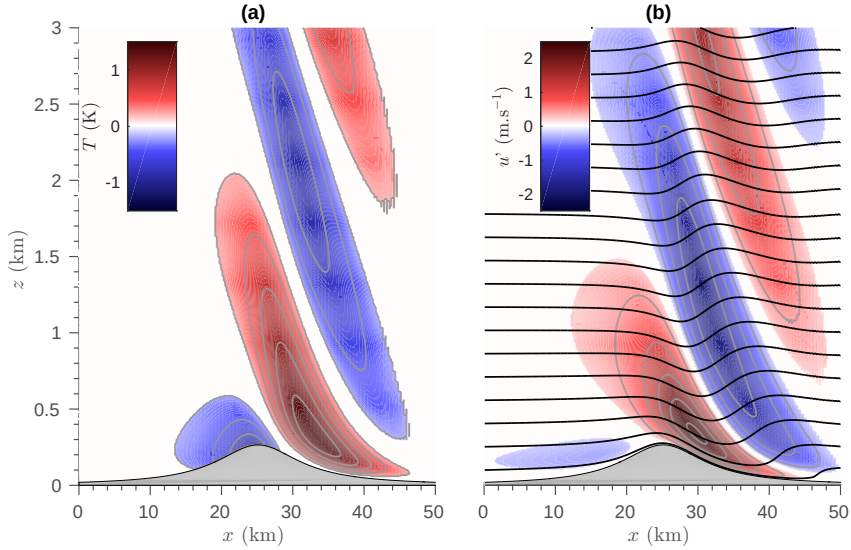

Figure 1: (a) Temperature fluctuations T' and (b) horizontal wind fluctuations u' resulting from interaction between a mountain and an incoming boundary layer. The streamlines are given by black lines superimposed to the wind fluctuations. The dimensionless parameters used are $H_N = 0.5$ and $J = 1.5$. The mountain is represented in gray.

we obtain $J = 1.5$, which corresponds to a moderately stable situation. Finally, the dimensionless value $H_N = 0.5$ is sufficiently small to guarantee that the near-linear mountain flow theory applies and produces realistic downslope winds and Foehn.

Figure 1a and 1b show the temperature and wind fluctuations produced by the mountain flow model, respectively. In figure 1a we observe that the strongest temperature anomaly is reached on the lee side, which is the "Foehn" effect. Figure 1b shows that the wind intensity on the lee side is larger than that on the windward side, which is characteristic of downslope

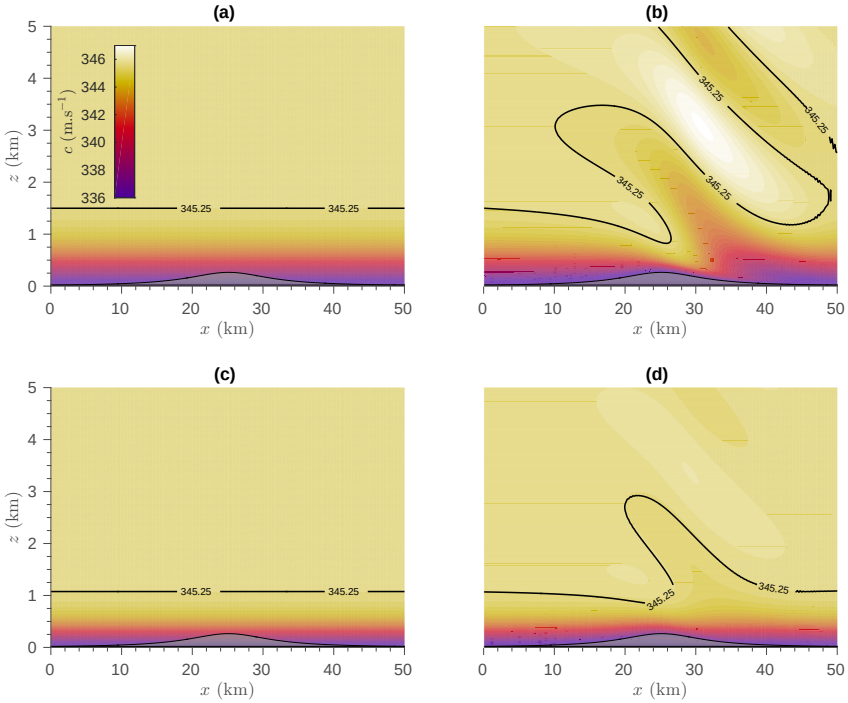

Figure 2: Effective sound speed field without (a,c) and with (b,d) interaction between a mountain and an incoming boundary layer. The dimensionless parameters used are $H_N = 0.5$ (a,b,c,d) and $J = 1.5$ (a,b) or $J = 0.5$ (c,d).

windstorms. The streamlines are represented in figure 1b to illustrate the so-called isentropic drawdown mechanism often used to explain Foehn. In this dry mechanism the Foehn results from warm air masses that slightly ascend on the windward side before descending abruptly on the leeward side. From Lott[29] we know that this effect and the intensity of the downslope winds are not that strong for significantly smaller values of J.

Figure 2 shows various effective sound speed fields that will be used in sections IV

194 and V. In figure 2a,c we just keep the incident waveguide unaltered and chopped it by the
195 mountain height for $J = 1.5$ (figure 2a) and $J = 0.5$ (figure 2c). This is representative of the
196 "mask" technique used in the literature[2], and to which we will systematically compare our
197 results to in the following. From figure 2a we can expect its effect to be substantial since
198 this mask potentially excludes from trapping all the waves with phase speed between around
199 336 m.s^{-1} and 339 m.s^{-1}. This exclusion is not as strong when the mountain wave field is
200 included as figure 2b shows, and indeed the effective sound speed "follows" the ground as
201 the air passes over the mountain (see, for instance, isoline $c = 336$ m.s^{-1}). Nevertheless,
202 it is clear that even in this case, the depth of the lower atmospheric duct substantially
203 decreases as we move from the upstream side of the mountain to its top. This shrinking also
204 manifests on the lee side, before that the flow reaches an abrupt expansion at around mid-
205 slope to return to its upstream depth. Hence, for lower altitudes, these two effects produce
206 a waveguide contraction as the flow passes over the mountain. Far above the mountain, the
207 disturbances take the form of gravity waves that propagate upward. In the effective sound
208 speed approximation framework, these gravity waves may be regarded as several acoustic
209 waveguides in which relatively low-frequency acoustic waves can potentially propagate.

210 It is worthwhile noting that both the distorsion of the low level waveguide and the
211 mountain wave field are not as intense for less stable situations (e.g. $J = 0.5$, figure 2d).
212 This is consistent with the fact that large values of J favor downslope winds and Foehn.

Comparison with the "mask" technique (figures 2c,d) demonstrates that for $J = 0.5$ the lowest effective sound speed isoline follows the global curvature of the terrain, instead of being chopped by the mountain. As discussed in section IV, this effect helps infrasound signals to travel across the hill.

III. Acoustic propagation in range-dependent media

A. Normal mode approach

The approach follows the formulation of the initial-value problem adopted by Bertin *et al.*[6], among others, for range-dependent environments. Assuming that the modes couple *adiabatically*[24], the solution for the Fourier transform $\tilde{p}(z;x,\omega)$ of the infrasound pressure fluctuations can be written as

$$\tilde{p}(z;x,\omega) \sim \sum_j \frac{a_j(\omega)\phi_j(z;x,\omega)}{\sqrt{k_j(x,\omega)}} \mathrm{e}^{i\theta_j(x,\omega)}, \tag{10}$$

where ϕ_j, k_j, a_j and θ_j are respectively the jth mode function, the corresponding modal wave number, amplitude and phase function. For a localized point-source at $x = z = 0$ that emits a signal $s(t)$ we simply have $a_j(\omega) = \phi_j(0;0,\omega)$, and the pressure fluctuation reads as

$$p(z;x,t) = \frac{1}{2\pi} \int_{-\infty}^{\infty} \tilde{s}(\omega)\tilde{p}(z;x,\omega)\mathrm{e}^{-i\omega t}\,\mathrm{d}\omega, \tag{11}$$

where $\tilde{s}(\omega)$ is the Fourier transform of $s(t)$. For convenience, we denote the derivative of $\theta_j(x,\omega)$ by $k_j(x,\omega)$ and the frequency dependence is dropped for conciseness. Physically k_j is the local (acoustic) wavenumber and the local phase speed is given by $c_j = \omega/k_j$.

229 It is worth noting that the pressure fluctuation can generally be decomposed into prop-
230 agating modes (along the x-axis direction) and evanescent modes, for which the imaginary
231 part of θ_j is positive. Far downstream of the acoustic point-source, at a distance large
232 compared to the wavelength, the evanescent modes are negligible and (10) is the correct
233 expression to consider.

234 Substitution of (10) into the classical Helmholtz equation gives, to order unity,

$$\frac{\partial^2 \phi_j}{\partial z^2} + \left[\frac{\omega^2}{c^2} - k_j^2\right] \phi_j = 0, \tag{12}$$

235 with the Neumann boundary condition expressing that the derivative of ϕ_j at $z = h(x)$ van-
236 ishes. For unbounded boundary layers, (12) must be supplemented by requiring a bounded-
237 ness or outgoing-wave condition as $z \to \infty$. The solution of (12) then becomes $p \sim \mathrm{e}^{-\mu_\infty z}$ as
238 $z \to \infty$, with the square-root function

$$\mu_\infty(k) = \left[k^2 - \frac{\omega^2}{c_\infty^2}\right]^{\frac{1}{2}}, \tag{13}$$

239 and c_∞ denotes the effective sound speed in the limit $z \to \infty$. The function (13) depends
240 on the variable k. Thus in the complex k-plane the branch cuts are to be inserted such that
241 $-\pi/2 < \arg(\mu_\infty) \leq \pi/2$. This choice of the branch cuts assures that as $z \to \infty$ the solution
242 of (12) either goes to zero or represents an outgoing wave for all values of k in the complex
243 plane.

244 The branch cuts extend from the branch points $k = \omega/c_\infty$ and $k = -\omega/c_\infty$ to infinity in

the complex k-plane. Over the initial region, far upstream of the mountain, the gravity wave field vanishes and we have $c_\infty = c_0 + U_0$, whereas at ground-level the effective sound speed reaches its minimum $c(0,0) = c_0$. For a right-propagating wave the condition of trapping therefore imposes that the initial eigenvalues k_j lie initially along the interval $c_0 < \omega/k < c_0 + U_0$. As each mode propagates downstream both the vertical sound speed profile and the branch points $\omega/c_\infty(x)$ vary, and the local eigenvalues $k_j(x)$ slowly adapts to these changes. In this process, the phase velocity of some acoustic modes eventually becomes larger than c_∞ and the associated trajectories terminate at a branch cut. Since it is not allowed to cross the branch cut it is therefore not possible to continue the eigensolution downstream of this point (and still satisfy the boundedness condition as $z \to \infty$). Therefore the corresponding modes are simply suppressed from the expansion (10).

In this work, the eigenfunctions and eigenvalues of (12) are calculated at a discrete set of ranges $x = x_n$ using the finite difference scheme used by Waxler *et al.*[48], among others. The eigenvalues are obtained using a QR decomposition for $x = 0$ and, for other ranges, the eigenvalues are tracked by using an iterative approach.

Since eigenfunctions are determined only up to a multiplicative constant, for definiteness we impose the normalization condition[24]

$$\int_{h_n}^{\infty} \phi_j^2(x_n, z)\, \mathrm{d}z = 1, \tag{14}$$

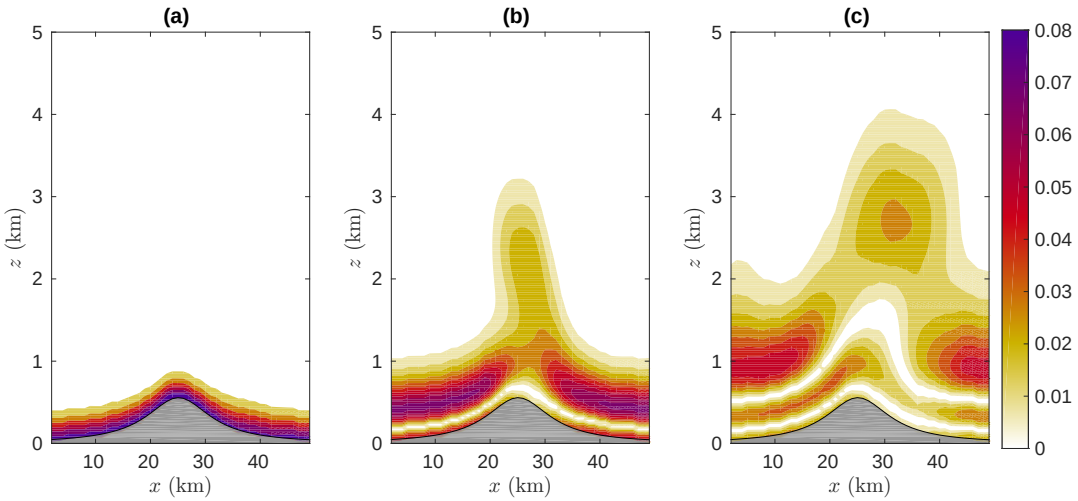

Figure 3: Eigenfunctions $|\phi_j|$ as functions of x and z for the first three modes (from left to right), and for a fixed frequency of 2.8125 Hz. The background state is computed for $H_N = 0.5$ and $J = 1.5$ (cf. figure 2b). (a) $j = 1$, (b) $j = 2$ and (c) $j = 3$.

where $h_n = h(x_n)$, together with the orthogonality condition

$$\int_{h_n}^{\infty} \phi_j(x_n, z)\phi_l(x_{n+1}, z)\,\mathrm{d}z = \delta_{jl}. \tag{15}$$

Anticipating the presence of upper level waveguides, the upper bound of integrals (14) and (15) was set to a sufficiently large value z_{top} and the effective sound speed profile $c(x_n, z)$ was smoothly continued to higher altitudes when necessary. To assess the validity of the numerical results, it has been checked that the eigenvalues were not sensitive to changes in z_{top}, or to the choice of the continuation of $c(x_n, z)$ above z_{top}.

For illustrative purposes, figure 3 shows the eigenfunctions of the first three modes as x increases along the source-receiver path, for a fixed frequency $\omega_0 = 2\pi \times 2.8125$ rad.s^{-1}. For

this frequency, these modes carry the dominant part of sound intensity over long distances and the expansion (10) can be truncated to $j \leq 3$, as discussed by Bertin *et al.*[6]. The first mode (figure 3a) is weakly sensitive to changes of the atmospheric flow as x varies. The other two modes in figures 3b,c are clearly affected by the presence of gravity waves and indeed, ground-based attenuation is clearly visible in the vicinity of the ridge top elevation. Furthermore, figure 3c shows that the presence of mountain waves aloft allows the modes to be trapped in an upper duct. This result is discussed further in section IV.

B. WKB treatment of the low-level waveguide

To distinguish the effect due to the boundary layer shrinking from that due to the mountain wave at upper levels, and to gain insight onto the behavior of the trapped modes, we have obtained solutions to (12) using the following profile of effective sound speed

$$\overline{c}(z) = \overline{c}_0 + \overline{c}_1 \tanh\left[z/\overline{\delta}\right], \tag{16}$$

and the WKB approximation of (12). In (16) the parameters $\overline{c}_0$, $\overline{c}_1$ and $\bar{\delta}$ are chosen to minimize the integrated squared error between c and $\bar{c}$ over the domain $h < z < z_{\max}$, where $z_{\max}$ is the depth of the low level waveguide, e.g. the lowest altitude such that

$$\frac{dc}{dz}(z_{\max}) = 0. \tag{17}$$

This definition ensures that the mountain wave is filtered out from the sound speed field and that the resulting waveguide width $z_{\max}$ varies slowly in the flow direction, as required by

the classical asymptotic methods for modeling infrasound propagation[24].

For fixed x, the filtered effective sound speed $\bar{c}$ in (16) is a strictly decreasing function of height and thus, $\omega^2/\bar{c}^2 - k^2$ is a continuous function which involves a single turning point[5] at $z = z_0(k)$. This choice allows us to use the Langer's formula[26] to build the uniformly valid WKB approximation

$$\bar{\phi}(z) = 2\sqrt{\pi}C \left[\frac{3}{2}\frac{S_0(z)}{\mu^3(z)}\right]^{\frac{1}{6}} \mathrm{Ai}\left\{\left[\frac{3}{2}S_0(z)\right]^{\frac{2}{3}}\right\}, \tag{18}$$

where Ai is the Airy function, and where the phase is given by

$$S_0(z) = \int_{z_0}^{z} \mu(s)\,\mathrm{d}s, \tag{19}$$

and the turning point z_0 is the unique root of $\mu(z_0) = 0$, where

$$\mu(z) = \left[k^2 - \frac{\omega^2}{\bar{c}^2(z)}\right]^{\frac{1}{2}}. \tag{20}$$

To ensure that the boundary condition at $z \to \infty$ is satisfied, the branch cuts are defined as for the function (13). Hence, using the leading asymptotic behavior of the Airy function for large z, (18) may be approximated by $\bar{\phi} \sim C\sqrt{\mu}\mathrm{e}^{-S_0}$, which is the leading order of the classical WKB approximation and the constant C is determined by the normalization condition (14). It is important to point out at this time that this normalization condition plays a central role, especially when estimating the ground-based pressure $\bar{\phi}_j/\sqrt{k_j}$ as x varies. In many cases, it can easily be verified that the closer to the ground the turning point is located, the greater the amplitude of the pressure field at ground level.

Below the turning point, the path of integration must be deformed such that the square-root function is continued into $\mu^2 = -\mu^2 \mathrm{e}^{i\pi}$ for $z < z_0$. On substituting this into (19), we note that $S_0^{2/3}$ is large and negative, and (18) can be simplified for $z \ll z_0$ by using the asymptotic behavior of the Airy function for negative argument[1]. To leading order, (18) may then be written as

$$\bar{\phi}(z) \sim 2C \left[-\mu^2(z)\right]^{-\frac{1}{4}} \cos\left\{\int_z^{z_0} \left[-\mu^2(s)\right]^{\frac{1}{2}} \,\mathrm{d}s - \frac{\pi}{4}\right\}. \tag{21}$$

Now for $z = h$, on account of the (Neumann) boundary condition $\bar{\phi}_z(h) = 0$, we obtain the constraint

$$\int_h^{z_0(k)} \sqrt{-\mu^2(s)}\,\mathrm{d}s = \frac{\pi}{4} + j\pi, \tag{22}$$

where j is a nonnegative integer. Since μ^2 depends on k, it appears that (22) determines the approximate value of k_j. In other words (22) defines the local dispersion relation where the streamwise station x only appears as a parameter (which is not specified here for conciseness).

As an additional bonus, equation (22) may be used to evaluate the effect of either downslope winds or mountain height on the local wavenumber. Upon totally differentiating the implicit function (22) for fixed ω, and equating to zero, we obtain

$$\frac{\mathrm{d}k}{\mathrm{d}x} = -\frac{\displaystyle\int_h^{z_0} \frac{\omega^2 \bar{c}_x}{\bar{c}^3\sqrt{-\mu^2}}\,\mathrm{d}s + \frac{\mathrm{d}h}{\mathrm{d}x}\sqrt{-\mu^2(h)}}{\displaystyle\int_h^{z_0} \frac{k}{\sqrt{-\mu^2}}\,\mathrm{d}s}, \tag{23}$$

Where the terms of this ratio are the derivatives of (22) with respect to k and x and $\bar{c}_x$ is the

derivative of $\bar{c}$ with respect to x. Similarly, we use the notations k_x and h_x for the derivatives of k and h with respect to x, respectively. Application of (23) for $\bar{c}_x > 0$ and $h_x > 0$ leads to $k_x < 0$. This means that the phase speed ω/k increases as the flow speeds up or when h increases.

IV. Impact of mountain waves on the normal modes

In order to obtain the pressure signal from (10), the modal wave numbers k_j, or equivalently the phase velocities $c_j = \omega/k_j$ are required. For range-dependent environments, these quantities are obtained as functions of ω and x either by solving (12) numerically or by using the WKB approximation, as described in section III.B. Figure 4 show contours of the phase velocity in the (ω, x)-plane for the first three modes [$j \leq 3$ in (10)] and the two effective sound speed fields considered in figures 2a and 2b. In figures 4a,b,c the numerically obtained results are represented in colors, when the mountain "mask" is applied, and the black curves give the corresponding WKB values. Figures 4d,e,f show the results obtained when the mountain flow dynamics is considered. Two important curves are also plotted as red and blue curves. These curves are obtained for each eigenvalue by decreasing ω, the location x being fixed. Starting from an initial value, the phase velocity c_j increases up to the maximum sound speed $c_{\max}$ as ω decreases. This behavior allows to identify the so-called cut-off frequency of the low-level waveguide, for which we have $c_j(x, \omega) = c(x, z_{\max})$, and which is referred to as $\omega_j^+(x)$ in the following (blue curve). For $\omega = \omega^+$ the eigenvalue obtained

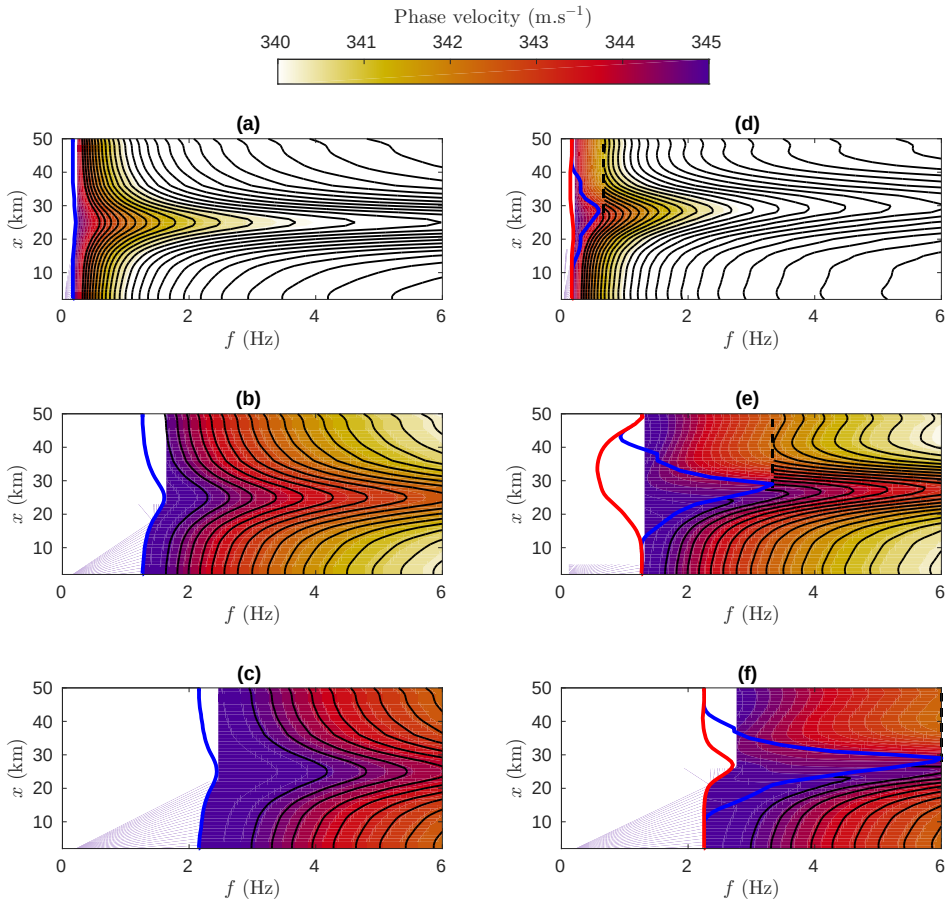

Figure 4: Phase velocity c_j for the first three modes (from top to bottom) as a function of streamwise location and frequency, for $H_N = 0.5$ and $J = 1.5$. (a,d) $j = 1$; (b,e) $j = 2$; (c,f) $j = 3$. The results obtained by applying a "mask" onto the effective sound speed field are given on the left (a-c). The figures on the right (d-f) show the impact of mountain wave dynamics. Black, red and blue curves give the WKB prediction and the cut-off frequencies ω^- and ω^+ as defined in section IV.

from (22) crosses a branch cut of (13) and thus, the WKB approximation fails to give a result for $\omega < \omega^+(x)$. Physically this condition may be interpreted as the requirement that the mode is not to be trapped in the low level duct. On the other hand the eigenvalue can be computed directly from (12) for lower frequencies, so that the eigenvalue reaches a terminal value for which we have $c_j(x,\omega) = c_{\max}(x)$. This value is referred to as $\omega_j^-(x)$ (red curve). It turns out that ω^- is not defined when considering the "mask" effect alone (figures 4a,b,c), essentially because in this case we have a single waveguide. Therefore, when mountain waves are present (figures 4d,e,f), the region $\omega_j^- < \omega < \omega_j^+$ corresponds to frequencies for which the eigenfunction ϕ_j penetrates up to the moutain wave field and can be confined within an upper level waveguide, as depicted in figure 3c for x lying in the range 25-35 km. This is an indication that at sufficiently low frequencies strong interaction between modes and mountain waves may occur.

As detailed in section III.A, a mode is not allowed to cross the branch cut, a situation that occurs for $\omega < \omega^-(x)$. The basic problem here is that as soon as the phase velocity of the locally wave solution becomes larger than the maximum effective sound speed, it is not possible to find a solution that remains bounded in the limit $z \to \infty$. Within the framework of slowly varying media, this condition translates into $a_j(\omega) = 0$ for $\omega < \omega^-(0)$. Physically this condition may be interpreted as the requirement that the mode does not propagate along the source-receiver path, for $x > 0$. The corresponding regions in the (ω, x) plane are

represented by blank areas in figures 4d,e.

For fixed but quite high frequencies (greater than 1 Hz typically), the phase velocity of the first mode, which is also the slowest mode (figure 4a,d), increases as we approach the ridge before decreasing in the lee side. Although this effect is less strong in presence of moutain flow, this behavior can be captured qualitatively using the "mask" technique and the WKB approximation. In fact this mode, which is confined in the vicinity of the ground, find its way through the ridge, even when the waveguide is substantially shrinked by mountain wave dynamics (figure 4d) or chopped by the ridge (figure 4a). The excellent agreement with the WKB approximation suggests that the mode essentially adjusts to the vertical shrinking of the waveguide, the increasing in its phase velocity being correctly predicted by equation (23) with $\bar{c}_x = 0$. For lower frequencies (less than 1 Hz), the discrepancies between the results obtained with the "mask" technique and the mountain flow are more pronounced, and essentially occur in the region where the low level duct fails to trap the modes, e.g. when lines of constant phase velocity intersect the blue curve. This is detailed in the following for the next two modes. For $j = 1$, we observe an overall agreement between the results obtained by solving (12) numerically or by using the WKB approximation. From a practical standpoint, this demonstrates that the interaction between infrasound and mountain flows can adequately be predicted at a low numerical cost, through finding the first maximum in the local effective sound celerity and using the WKB approximation. This approach,

however, is justified only if we can neglect the contribution of other modes ($j > 1$).

In computing the phase velocity for the other modes ($j > 1$), we observe that the mask technique fails in predicting important changes. Primarily, figures 4b,c show that the cut-off frequency ω^+ substantially increases as we approach the ridge top, and reaches its maximum at $x_0 = 25$km. As discussed in section III.A, when the condition $\omega < \omega^+(x_0)$ is satisfied downstream x_0, the mode is simply suppressed. In presence of mountain waves (figures 4e,f) the low level waveguide is extremely shrinked, and the penetration of $\omega^+(x)$ into the (ω, x)-plane is very pronounced. This effect is essentially due to Foehn, which shifts the maximum cutt-off frequency $\omega^+(x)$ on the leeward side of the ridge, at a distance of approximately 30 km (figure 4e,f). Hence, immediately downstream this location, the mode obtained with the one-turning-point WKB approximation (*i.e.* when mountain waves are filtered out) must be suppressed, as shown in figures 4e,f. This is not the case when mountain waves are considered and indeed, the fact that the mode remains propagating in the horizontal direction for $x > x_0$ is essentially due to the emergence of multiple possible upper ducts above the mountain. For $j = 2$, we even see that the cut-off frequency of the upper duct ω^- decreases as we pass over the ridge and thus, the contribution of the mode has to be maintained in (10). This finding is in strong contrast with that obtained using the "mask" technique. On the other hand, and for $j = 3$, figure 4f shows that ω^- increases as we move closer to the ridge. This means that the mountain wave pattern failed in ducting the

391 mode that escapes from the low-level duct. Finally it is important to notice that for smaller
392 values of J (H_N being constant), the boundary layer tends to follows the global curvature
393 of the terrain, thereby yielding a significant number of modes to travel over the mountain,
394 whereas the upper bound ω^+ obtained with the "mask" technique penetrates much more
395 into the (ω, x)-plane.

396 Figure 5 shows the sound intensity $|\phi_j/\sqrt{k_j}|$ at ground level $z = h(x)$, as a function of x
397 and ω, for the first three modes. The magnitude of the contours are labelled in decibel, with
398 a reference sound intensity computed at $x = 0$. Results are given for the two effective sound
399 speed profiles defined above and depicted in figures 2a,b. The contours in color are for the
400 results obtained by solving numerically (12), and the black curves give the one-turning-point
401 WKB approximation. Red curves and blue curves represent the cut-off frequencies ω_j^- and
402 ω_j^+, as in figure 4. Figures 5d,e,f, essentially show strong attenuation in the region $\omega_j^- < \omega <$
403 ω_j^+. These attenuations are due to strong interactions between the acoustic waves and the
404 mountain waves, the latter creating new acoustic waveguides at higher altitudes, as discussed
405 previously. The energy leaks that follow the tunneling effect for sound waves (cf. figure 3b,c)
406 and the standard requirement that the integral of ϕ_j^2 is fixed to one [condition (14)], lead
407 to strong attenuations at ground level. These attenuations are more pronounced for higher
408 indices, simply because the corresponding turning points, at $x = 0$, are closer to $z_{\max}$.
409 Since the phase velocity adapts to the local environment encountered by the sound wave,

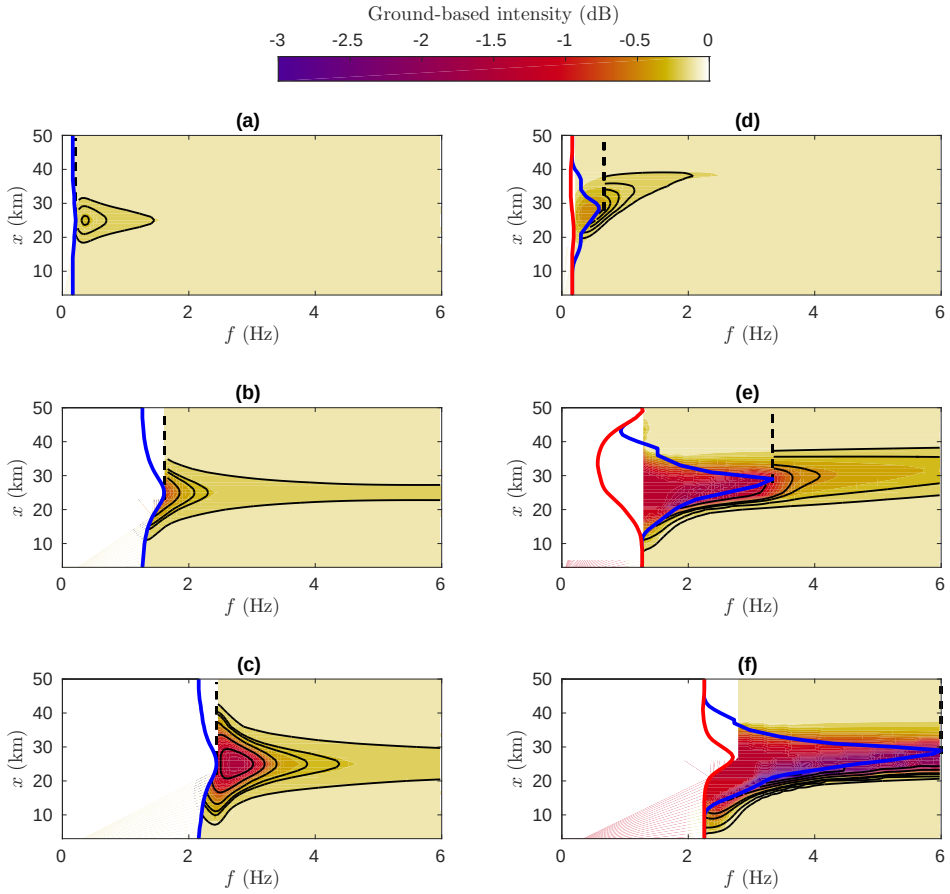

Figure 5: Ground-based sound intensity $|\phi_j/\sqrt{k_j}|$ for the first three modes as a function of streamwise location and frequency, for $H_N = 0.5$ and $J = 1.5$. (a,d) $j = 1$; (b,e) $j = 2$; (c,f) $j = 3$. The WKB prediction is superimposed in black contours. Red and blue curves correspond of those of figure 4.

the highest modes are more likely to leave the low-level waveguide.

While the ground-based attenuation of sound intensity can be qualitatively understood when the mode shifts to upper-level waveguides (for $\omega_j^- < \omega < \omega_j^+$), it is less clear why

it occurs when the waveguide shrinks, as figures 5a,b,c show for $\omega > \omega^+$. This behavior appears to contradict the normalization requirement, which *a priori* results in surface amplifications rather than surface attenuations. However, using the WKB approximation, the apparent contradiction is resolved by the recognition that the proper measure of the size of the dispersive region, $z_0 - h$ is always smaller than its value at $x = 0$. Based on the above discussions, clearly the surface attenuation is a combination of the emergence of upper-level waveguides as well as depth reduction of the low-level waveguide.

V. Impact of mountain waves on signals

In the previous section we have seen how the normal modes, in which the structure over the whole (ω, x)-plane can be delineated, are attenuated by mountain waves, and we have given a general condition by which this interaction can be characterized, in terms of the cut-off frequencies ω^- and ω^+. To measure the extent to which these effects are significant when the sources of infrasound are localized in both space and time, we next calculate ground-based waveforms, using the FFT algorithm[7]. A source function is introduced in the form

$$s(t) = K\mathrm{e}^{-\frac{t-T_0}{\sigma^2}} \cos(2\pi f_c t), \tag{24}$$

where $T_0 = 10$ s, $f_c = 3$ Hz and $\sigma = 1/5$. The parameters are adjusted such that the maximum frequency is 6 Hz, with a leading frequency of 3 Hz. K is a suitable coefficient that yields a normalized pulse. This source transfers most of its energy onto the first three

modes [$j \leq 3$ in (10)] which are the modes of greatest contribution when the frequency is relatively low. For this reason, the modal expansion is truncated to these modes in the following.

The normalization of signals obtained for different locations downstream the mountain is fixed so that the amplitudes can be compared to each other. The global effect of the mountain can be summarized by means of the attenuation

$$1 - \frac{I(x)}{I_0(x)}, \tag{25}$$

where the sound intensity at ground level ($z = h$) is defined as

$$I(x) = \int_0^\infty [p(h; x, t)]^2 \, \mathrm{d}t, \tag{26}$$

where the waveform $p(h; x; t)$ is obtained from (11) and (10), with $j \leq 3$, and by solving the Helmholtz equation (12) numerically. Here I_0 is a reference sound intensity obtained by taking $x = 0$ in (26). This choice allows the results to be compared with the classical mountain-free range-independent case (*i.e.* when the effective sound speed is given by $c_0 + U(z)$), which is used in the infrasound research community.

In this section, we proceed systematically and vary the Richardson number between 0.25 and 2 and the non-dimensional mountain height H_N between 0.2 and 0.8. As discussed in section IV, the sound speed modifications are intimately linked to the mountain flow situations. To measure the downslope wind amplitude and Foehn, and following Lott[29], we

447 use

$$A = \max_{\substack{2z<H_N \\ 0<x<2F}} \left[\frac{u'(x,z)}{U(H)} \right], \tag{27}$$

448 which is the maximum of the ratio between the horizontal wind disturbance along the foothill
449 and the background wind at the top of the hill. Typically, when A approaches and exceeds 1,
450 the dynamics induces wind amplitudes that are either equal to or exceed the amplitude of
451 the winds at the summit of the ridge. In other words, the flow speeds up along the ridge,
452 and this occurs easily for $J > 1$.

453 Before proceeding systematically we present here three cases that illustrate the general
454 results that will conclude the paper. Case I is defined by $\delta = 600$ m and $H = 250$ m,
455 which corresponds to a relatively small mountain and a pronounced shear. In terms of
456 dimensionless parameters, we have $J = 0.75$ and $H_N = 0.3$ so that the downslope wind
457 amplitude is $A = 0.75$. Case II is associated with a larger depth $\delta = 1$ km and a higher
458 mountain $H = 600$ m. The corresponding dimensionless parameters are given by $J = 2$ and
459 $H_N = 0.8$ so that $A = 3$, which reflects intense downslope winds. In order to estimate the
460 role of stability, we keep $H_N = 0.8$ and consider a much less stable flow with a Richardson
461 number $J = 0.3$, as a third Case III. This last case corresponds to a situation for which we
462 have $H/\delta = H_N/\sqrt{J} \simeq 1.5$ and thus, we can expect that most of the modes are obstructed
463 by the mountain when the "mask" technique is used.

464 The resulting acoustic signals associated with cases I, II and III are shown in figure 6

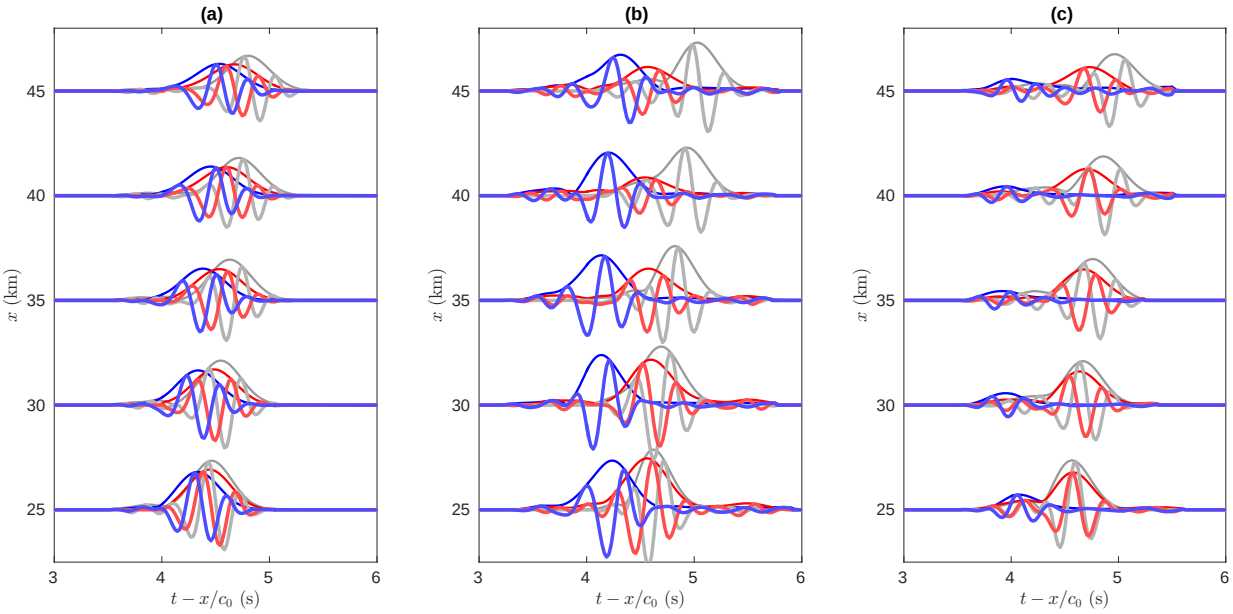

Figure 6: Waveforms obtained for cases I (a), II (b) and III (c) as functions of the retarded time $t - x/c_0$ without (blue) and with (red) interaction between the mountain and the boundary layer. The signals obtained for an unperturbed range-independent case (without mountain and mask) are plotted in gray, for reference. Case I: $J = 0.75$ and $H_N = 0.3$; case II: $J = 2$ and $H_N = 0.8$; case III: $J = 0.3$ and $H_N = 0.8$. The source is defined by (24).

for different locations downstream the mountain. The blue and red colors correspond to waveforms computed by applying the "mask" technique and by solving mountain flow dynamics, respectively. Waveforms obtained for the unperturbed range-independent profile $c_0 + U(z)$ are plotted in gray. The envelope of signals is plotted in thinner line, using the Hilbert transform. Figure 6 shows evidence that the interaction between the mountain flow

and the acoustic wave may give rise to attenuation or amplification of ground-based signals, depending on the Richardson number. While the impact of the mountain on the ground-based signals is moderate for Case I (figure 6a), for which the attenuation does not exceed 13%, Case II (figure 6b) gives rise to attenuations as large as 48% at $x = 40$ km. This attenuation is mainly due to the fact that the first mode is no longer trapped in the low level waveguide and thus, a large part of the energy is lost at higher altitudes through interactions with mountain waves. On the other hand, case III (figure 6c) shows that the mountain wave dynamics may favor the passage of acoustic waves, mitigating the "mask" effect. The essential constrast with Case II is that, despite a strong reduction of its height, the incoming waveguide slips over the mountain rather than being destroyed over the winward side. The acoustic path then follows the global curvature of the terrain and the sound intensity is 80% larger than that obtained with the "mask" technique.

As discussed above, the signals obtained for the three cases considered in figure 6 do not cover all situations. In order to estimate how the mountain wave dynamics impacts the infrasound measurement, the ground-based attenuations (25) are first computed as functions of x, and then averaged over two intervals $x_0 < x < x_1$ and $x_1 < x < x_2$, with $x_0 = 25$ km, $x_1 = 40$ km and $x_2 = 50$ km. The process is repeated for different values of J and H_N so as to obtain a complete portrait of averaged attenuations in time domain. Figures 7 and 8 show typical results for the first and second intervals, respectively. The first interval

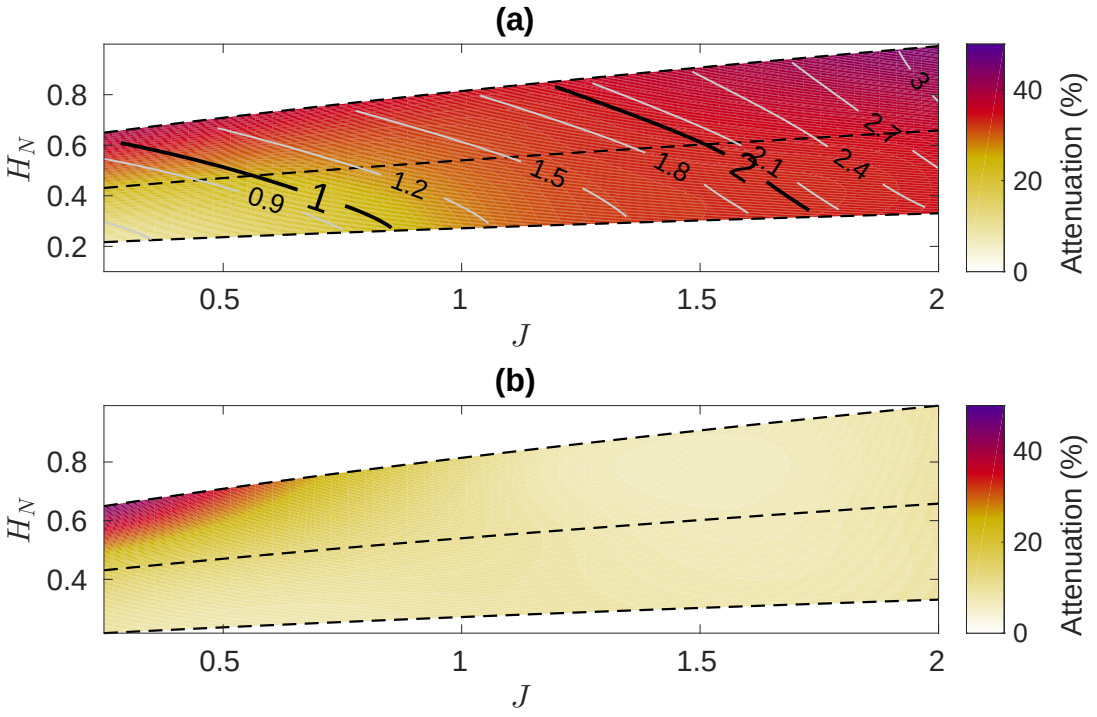

Figure 7: Far-field averaged attenuation downstream the mountain, in the range $25-40$ km as a function of J and H_N with mountain wave disturbances (a) and the "mask" effect alone (b). The downslope wind amplitude A is given by black and white contours.

$x_0 < x < x_1$ is adopted here to quantify the infrasound attenuation on the leeward flank of the ridge. Firstly, figure 7a shows that the mountain flow produces larger attenuations than that obtained with the "mask" technique (in figure 7b). Furthermore, even though the shrinking of the waveguide by the Foehn produces strong attenuations (A is almost everywhere larger than 1), a significant fraction of the attenuation is indeed associated

with sound propagation within upper level waveguides, through local adjustments of few normal modes, as discussed in length in section IV. This is typically the case for relatively large J ($J > 1.5$) and small H_N, in the range $0.2 < H_N < 0.4$. In this region the sound intensity on the lee-side flanck of the ridge is attenuated by a factor of 30% (figure 7a) and decreases down to about 20% far downstream (figure 8a). Secondly, comparisons of figures 7a and 7b show that at low Richardson numbers ($J < 0.5$) and for high mountains ($0.6 < H_N < 0.7$) attenuation is mainly due to the "mask" effect, which produces a strong reduction of the waveguide height. The second interval is used to capture the far-field sound attenuation downstream the mountain without including the constructive/destructive interference effects associated with local changes of phases. In fact, at about two or three mountain half-widths downstream of the maximum height location, the modes recover their initial characteristics for $x \to \infty$, unless they reach a branch cut as discussed in section II.A. Owing to these changes in the resulting modal expansion (10), a residual attenuation is expected far downstream the mountain. This attenuation is irreversible in the sense that the full set of eigenvalues at $x = 0$ is not recovered downstream the mountain. Comparison of figures 7a and 8a shows that this effect is apparent at relatively high Richardson numbers, in the top right corner of figure 7a. Finally, it is important to point out that another striking result here is that for large values of H_N and narrow waveguides (small J), the mountain flow dynamics favor infrasound propagation, as discussed in section IV.

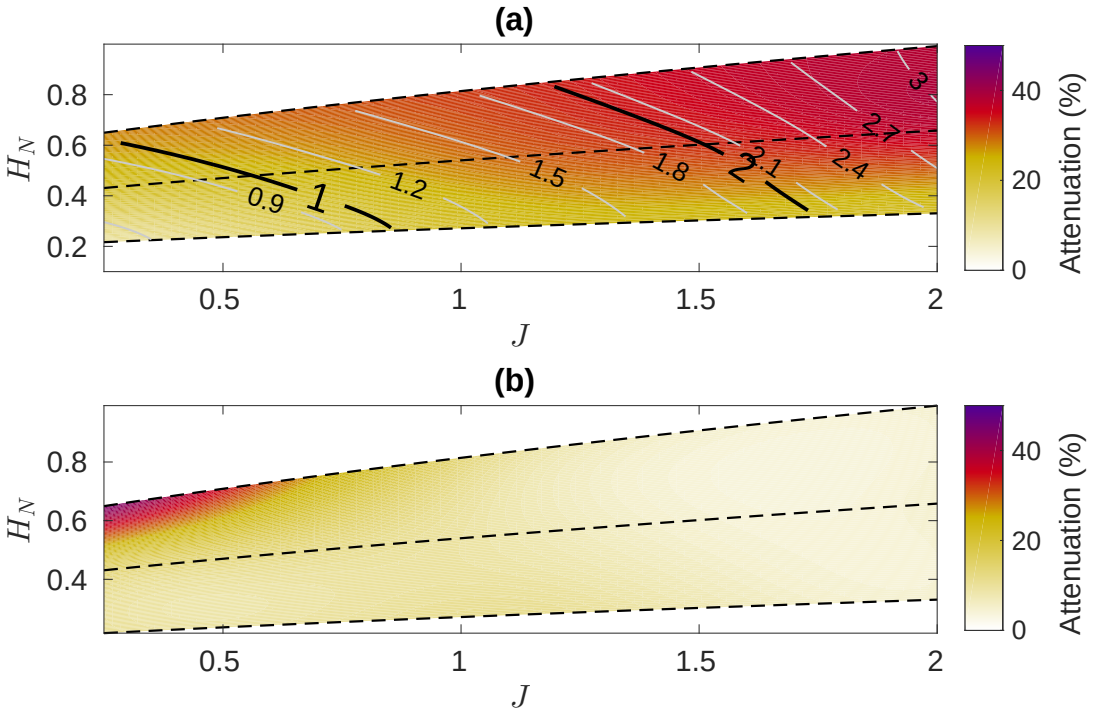

Figure 8: Far-field averaged attenuation, in the range $40-50$ km as a function of J and H_N with mountain wave disturbances (a) and the "mask" effect alone (b). The downslope wind amplitude A is given by black and white contours.

VI. Conclusions

In this paper, we have examined the propagation of sound within mountain flows. The mountain flow model is based on the integration of the linear inviscid Taylor-Goldstein equation, forced by a nonlinear surface boundary condition. To calculate infrasound signals,

we also used a range-dependent normal mode approach, which allows the decomposition of the acoustic pressure field into distinct normal modes. The basic assumption introduced in the present work is that the acoustic modes couple adiabatically, *i. e.* without any transfer of energy to higher or lower modes. Ground-based signals were computed using Fourier synthesis of frequency-domain solutions, for a given ground-based broadband acoustic source.

The central result of this paper is that mountain wave dynamics may lead to strong attenuation or amplification of upcoming acoustic waves, regarding to the direct "mask" effect the mountain has on acoustic propagation. For a stable flow ($J \geq 1$) the mountain wave dynamics produces large horizontal winds and buoyancy disturbances at low level that result in intense downslope winds and Foehn. When the downslope wind is less intense ($J < 1$), the flows can reinforce the acoustic waveguide over the mountain and lead to a signal of greater amplitude compared to that obtained by the "mask" effect. The acoustic waveguide is then strongly impacted which leads to a new kind of acoustic (reversible) absorption that can be related to local adjustments of few normal modes. It is worthwhile to point out here that acoustic absorption is mainly governed by the Richardson number, and more precisely by the critical value $J \simeq 1$, which is also a transition regime for mountain wave dynamics.

In striking contrast to this local behavior of acoustic modes is the sound attenuation far downstream from the mountain. This second type of absorption is due to irreversible

processes that are intimately connected to leaking modes along the source-receiver path. While leaking modes are known to play a role in the transient waveform, the classical practice is to neglect the contributions from these modes at large horizontal distances from explosions in the atmosphere. This approach, however, ignores range-dependence of the environment. These modes may be "activated" by a point-source in the form of classical waveguide modes and then decay exponentially with increasing distances far downstream from the mountain, as a result of the atmospheric state evolution. In this way, the corresponding component involving these modes vanishes far downstream from the mountain. This results in absorption farther downstream from the mountain, even though the background state recovers its initial state (e.g. upstream from the mountain).

The present work presents our current understanding of acoustic absorption due to mountain wave dynamics with emphasis upon a modal description of the acoustic field, including static stability effects. Though the present analysis does not answer all the questions regarding the complex phenomenon of absorption, it has shown how a range-dependent analysis can provide some insight into the interaction of acoustic waves and mountain wave fields. Other aspects that may give rise to additional dissipation have not been fully explored, such as, interaction of infrasound waves with ground and turbulence. However, the mountain wave model used in this study cannot predict the turbulence associated with GW breaking, a process that occurs for small J. While a rough estimate of the complex impedance effect

gives an absorption of 1 % for the cases considered in this study, the role of turbulence is more complex to quantify. The main difficulty is that the adiabatic approximation ceases to apply when the turbulence correlation length and acoustic wavelength are of the same order of magnitude. Some preliminary calculations have been made by the authors for estimating far-field absorption, using the techniques described in this paper, but with mode couplings and complex imaginary part of the grounding impedance. The results show good agreement with that obtained in the present work, except for cases where fine-grained turbulence dominates.

The present work is also related to the more general issue of incorporating unresolved GW variability in infrasound propagation calculations. Recent works[25;21;14] suggest that the mismatch between simulated and observed signals is related to the fact that the atmospheric specifications used in most studies do not adequately represent internal gravity waves. In the Atmospheric General Circulation Models which are used to produce the atmospheric specifications, these GWs are represented by parameterizations and in return, these parameterizations can be used to predict the GWs field used in infrasound studies. This is the approach followed by Drob *et al.*[14], in which the global spectral scheme of Hines[22] is used to estimate the effect of GWs on infrasound time arrivals. The interesting aspect of using the model proposed by Hines[22] is that it allows obtaining GW fields that give rise to the right climate[28].

REFERENCES

1. M. Abramowitz, and I. A. Stegun, Handbook of mathematical functions: with formulas, graphs, and mathematical tables, **Vol. 55**. *National Bureau of Standards Applied Mathematics Series* (**1964**), p. 1046.

2. J. D. Assink, G. Averbuch, P. S. M. Smets, and L. G. Evers, "On the infrasound detected from the 2013 and 2016 DPRK's underground nuclear tests", *Geophys. Res. Lett.*, **43**, 3526-3533 (**2016**).

3. J. D. Assink, R. Waxler, and D. Drob, "On the sensitivity of infrasonic traveltimes in the equatorial region to the atmospheric tides", *J. Geophys. Res. Atmos.*, **117**, D01110 (**2012**).

4. K. Attenborough, K. M. Li, and K. Horoshenkov, "Predicting outdoor sound", *CRC Press* (**2006**), p. 485.

5. C. M. Bender, and S. A. Orszag, Advanced mathematical methods for scientists and engineers I: Asymptotic methods and perturbation theory, *Springer Science and Business Media* (**2013**), p. 593.

6. M. Bertin, C. Millet, and D. Bouche, "A low-order reduced model for the long-range

propagation of infrasounds in the atmosphere", *J. Acoust. Soc. Am.*, **136(1)**, 37-52 (**2014**).

7. E. O. Brigham, and R. E. Morrow, "The fast Fourier transform", *IEEE spectrum*, **4(12)**, 63-70 (**1967**).

8. J. Candelier, S. Le Dizès, and C. Millet, "Inviscid instability of a stably stratified compressible boundary layer on an inclined surface", *J. Fluid Mech.*, **694**, 524-539 (**2012**).

9. W. Cheng, F., M. B. Parlange, and W. Brutsaert, "Pathology of Monin-Obukhov similarity in the stable boundary layer", *J. Geophys. Res.*, **110**, D06101 (**2005**).

10. G. Chimonas, and C. J. Nappo, " Wave drag in the planetary boundary layer over complex terrain", *Boundary-layer meteorology*, **47**, 217-232 (**1989**).

11. I. P. Chunchuzov, G. A. Bush, and S. N. Kulichkov, "On acoustical impulse propagation in a moving inhomogeneous atmospheric layer", *J. Acoust. Soc. Am.*, **88(1)**, 455-461 (**1990**).

12. I. Chunchuzov, S. Kulichkov, A. Otrezov, and V. Perepelkin, "Acoustic pulse propagation through a fluctuating stably stratified atmospheric boundary layer", *J. Acoust. Soc. Am.*, **117(4)**, 1868-1879 (**2005**).

606 **13.** F. Damiens, F. Lott, C. Millet, and R. Plougonven, "An adiabatic Foehn mechanism",
607 *Under consideration for publication in Quaterly J. of the Royal Meteorol. Soc.* (**2017**).

608 **14.** D. P. Drob, D. Broutman, M. A. Hedlin, N. W. Winslow, and R. G. Gibson, "A
609 method for specifying atmospheric gravity wavefields for long-range infrasound propaga-
610 tion calculations", *J. Geophys. Res. Atmos.*, **118(10)**, 3933-3943 (**2013**).

611 **15.** D. R. Durran, "Mountain waves and downslope winds". *AMS Meteorological Mono-*
612 *graphs*, **23**, 59-83 (**1990**).

613 **16.** J. A. Dutton, *Dynamics of atmospheric motion*, *Dover Publications, Inc., New-York*
614 (**1995**), p. 617.

615 **17.** D. Fee, R. Waxler, J. Assink, Y. Gitterman, J. Given, J. Coyne, P. Mialle, M. Garces,
616 D. Drob, D. Kleinert, and R. Hofstetter, "Overview of the 2009 and 2011 Sayarim infra-
617 sound calibration experiments", *J. Geophys. Res. Atmos.*, **118(12)**, 6122-6143 (**2013**).

618 **18.** D. C. Fritts, and M. J. Alexander, "Gravity wave dynamics and effects in the middle
619 atmosphere", *Rev. Geophysics*, **41**(1), 1003 (**2003**).

620 **19.** O. A. Godin, "An effective quiescent medium for sound propagating through an inho-
621 mogeneous moving fluid", *J. Acous. Soc. Am.*, **112**, 1269-1275 (**2002**).

622 **20.** E. E. Gossard, and W. H. Hooke, "Waves in the atmosphere: atmospheric infrasound

and gravity waves-their generation and propagation". *Elsevier Scientific Publishing Company* (**1975**), p. 456.

21. M. A. Hedlin, and D. P. Drob, "Statistical characterization of atmospheric gravity waves by seismoacoustic observations", *J. Geophys. Res. Atmos.*, **119(9)**, 5345-5363 (**2014**).

22. C. O. Hines, "Doppler-spread parameterization of gravity-wave momentum deposition in the middle atmosphere. Part 2: Broad and quasi monochromatic spectra, and implementation", *J. Atmos. Terr. Phys.*, **59(4)**, 387-400 (**1997**).

23. L. N. Howard, "Note on a paper of John W. Miles", *J. Fluid Mech.*, **10(04)**, 509-512 (**1961**).

24. F. B. Jensen, W. A. Kuperman, M. B. Porter, and H. Schmidt, Computational ocean acoustics, *Springer Science and Business Media* (**2011**), p. 794.

25. J. M. Lalande, and R. Waxler, "The interaction between infrasonic waves and gravity wave perturbations: Application to observations using UTTR Rocket Motor Fuel Elimination Events", *J. Geophys. Res. Atmos.*, **121(10)**, 5585-5600 (**2016**).

26. R. E. Langer, "The asymptotic solutions of ordinary linear differential equations of

639 the second order, with special reference to a turning point", *Trans. Amer. Math. Soc.*,
640 **67(2)**, 461-490 (**1949**).

641 **27.** R. R. Long, "Some aspects of the flow of stratified fluids; 1. A theoretical investiga-
642 tion", *Tellus*, **5**, 42-58 (**1953**).

643 **28.** F. Lott, and C. Millet, "The representation of gravity waves in atmospheric general
644 circulation models (GCMs)", *In Infrasound monitoring for atmospheric studies*, *Springer*
645 *Netherlands* (**2010**), pp. 685-699.

646 **29.** F. Lott, "A new theory for downslope windstorms and trapped mountain waves", J.
647 Atmos. Sci., **73(9)**, 3585-3597 (**2016**).

648 **30.** M. H. McKenna, R. G. Gibson, B. E. Walker, J. McKenna, N. W. Winslow, and A. S.
649 Kofford, "Topographic effects on infrasound propagation", *J. Acoust. Soc. Am.*, **131**(1),
650 35-46 (**2012**).

651 **31.** M. H. McKenna, B. W. Stump, and C. Hayward, "Effect of time-varying tropospheric
652 models on near-regional and regional infrasound propagation as constrained by observa-
653 tional data", *J. Geophys. Res.*, **113**, D11111 (**2008**).

654 **32.** J. W. Melgarejo, and J. W. Deardorff, "Stability functions for the boundary layer

655 resistance laws based upon observed boundary layer heights", *J. Atmos. Sci.*, **31**, 1324-
656 1333 (**1974**).

657 **33.** J. W. Miles, "On the stability of heterogeneous shear flows", *J. Fluid Mech.*, **10(04)**,
658 496-508 (**1961**).

659 **34.** C. Millet, J. C. Robinet, and C. Roblin, "On using computational aeroacoustics for
660 long-range propagation of infrasounds in realistic atmospheres", *Geophys. Res. Let.*,
661 **34(14)** (**2007**).

662 **35.** C. J. Nappo, H. Y. Chun, and H. J. Lee, "A parameterization of wave stress in the
663 planetary boundary layer for use in mesoscale models", *Atmos. Env.*, **38**, 2665-2675
664 (**2004**).

665 **36.** P. Queney, "The problem of air flow over mountains:A summary of theoretical studies",
666 *Bull. Am. Meteorol. Soc.*, **29**, 16-26 (**1948**).

667 **37.** H. Richner, and P. Hachler, "Understanding and forecasting alpine Foehn", *Mountain*
668 *weather research and forecasting: recent progress and current challenges*, F. K. Chow,
669 S. F. J. De Wekker, and B. J. Snyder, *Springer Science and Business Media*, 219-260
670 (**2013**).

671 **38.** P. Seibert, "South Foehn studies since the alpex experiment", *Meteorol. and Atmos.*
672 *Phys.*, **43**, 91-103 (**1990**).

673 **39.** R. B. Smith, "The influence of mountains on the atmosphere". *Adv. Geophys.*, **21**,
674 87-230 (**1979**).

675 **40.** R. B. Smith, B. K. Woods, J. Jensen, W. A. Cooper, J. D. Doyle, Q. Jiang, and V.
676 Grubisic, "Mountain waves entering the stratosphere", *J. Atmos. Sci.*, **65**, 2543-2562
677 (**2008**).

678 **41.** J. Sun, D.H. Lenschow, S.P. Burns, R.M. Banta, R.K. Newsom, R. Coulter, S. Frasier,
679 T. Ince, C. Nappo, B.B. Balsey, M. Jensen, L. Mahrt, D. Millar, and B. Skelly, "Atmo-
680 spheric disturbances that generate intermittent turbulence in nocturnal boundary layers",
681 *Bound.-Layer Meteor*, **110**, 255-279 (**2003**).

682 **42.** L. C. Sutherland, and H. E. Bass, "Atmospheric absorption in the atmosphere up to
683 160 km", *J. Acoust. Soc. Am.*, **115**(3), 1012-1032 (**2004**).

684 **43.** K. Szuberla, J. V. Olson, and K. M. Arnoult, "Explosion localization via infrasound",
685 *J. Acoust. Soc. Am.*, **125**(5), 112-116 (**2009**).

686 **44.** R. Waxler, "A vertical eigenfunction expansion for the propagation of sound in a

687 downward-refracting atmosphere over a complex impedance plane", *J. Acoust. Soc. Am.*,
688 **112**, 2540-2552 (**2002**).

689 **45.** R. Waxler, "Modal expansions for sound propagation in the nocturnal boundary layer",
690 *J. Acoust. Soc. Am.*, **115**, 1437-1448 (**2004**).

691 **46.** R. Waxler, C. L. Talmadge, S. Dravida, and K. E. Gilbert, "The near-ground structure
692 of the nocturnal sound field", *J. Acoust. Soc. Am.*, **119**, 86-95 (**2006**).

693 **47.** R. Waxler, K. E. Gilbert, and C. Talmadge, "A theoretical treatment of the long range
694 propagation of impulsive signals under strongly ducted nocturnal conditions", *J. Acoust.*
695 *Soc. Am.*, **124**, 2742-2754 (**2008**).

696 **48.** R. Waxler, J. Assink, and D. Velea, "Modal expansions for infrasound propagation
697 and their implications for ground-to-ground propagation", *J. Acoust. Soc. Am.*, **141**,
698 1290-1307 (**2017**).

699 **49.** C. D. Whiteman, and J. D. Whiteman, "An historical climatology of damaging downs-
700 lope windstorms at Boulder, Colorado", NOAA Tech. Report ERL336-APCL 35 (**1974**).

701 **50.** C. Whiteman, X. Bian, and S. Zhong, "Low-level jet climatology from enhanced raw-
702 insonde observations at a site in the southern great plains", *J. Appl. Meteorol.*, **36**,
703 1363-1376 (**1997**).